2018-03-02

Submesoscale Rossby waves on the Antarctic Circumpolar Current

Taylor, J

http://hdl.handle.net/10026.1/10752

Submesoscale Rossby waves on the Antarctic Circumpolar Current

John R. Taylor,[1]* Scott Bachman,[2] Megan Stamper,[1] Phil Hosegood[3], Katherine Adams[3], Jean-Baptiste Sallee[4], Ricardo Torres[5]

[1]Department of Applied Mathematics and Theoretical Physics, University of Cambridge, Centre for Mathematical Sciences, Wilberforce Road, Cambridge, UK

[2]National Center for Atmospheric Research, Boulder, CO, USA.

[3]School of Biological and Marine Sciences, Plymouth University, Plymouth, UK.

[4]Sorbonne Universites, UPMC/CNRS, LOCEAN Laboratory, Paris, France.

[5]Plymouth Marine Laboratory, Plymouth, UK.

*To whom correspondence should be addressed; E-mail: J.R.Taylor@damtp.cam.ac.uk.

One sentence summary: Submesoscale Rossby waves are found along Antarctic Circumpolar Current where they drive strong vertical circulations.

The eastward flowing Antarctic Circumpolar Current (ACC) plays a central role in the global ocean overturning circulation (*1*) and facilitates the exchange of water between the ocean surface and interior. Submesoscale eddies and fronts with scales between $1-10$ km are regularly observed in the upper ocean and are known to be associated with strong vertical circulations and enhanced stratification (*2, 3*). Despite their importance in other locations, comparatively little is known about submesoscales in the Southern Ocean. Here, we present results from new observations, models, and theory showing that submesoscales are qualitatively changed by the strong jet associated with the ACC in the Scotia Sea, east of Drake Passage. Growing submesoscale disturbances develop

along a dense filament and are transformed into submesoscale Rossby waves which propagate upstream relative to the eastward jet. Unlike their counterparts in slower currents, the submesoscale Rossby waves do not destroy the underlying frontal structure. The development of submesoscale instabilities leads to strong net subduction of water associated with a dense outcropping filament, and later the submesoscale Rossby waves are associated with intense vertical circulations.

The ACC transports water between the major ocean basins and forms the linchpin of the global Meridional Overturning Circulation (*1*). The ACC is composed of a series of interconnected jets, each associated with abrupt changes in density, or fronts. The Subantarctic Front (SAF) and Polar Front (PF) are the strongest climatological fronts associated with the ACC. Here, deep density surfaces (or isopycnals) outcrop to the sea surface, providing a pathway along which water can upwell to the ocean surface, exchange heat, carbon, and oxygen with the atmosphere, and return to the ocean interior (*4*). Indeed, the Southern Ocean is a significant sink for anthropogenic carbon and heat (*5, 6*). Southern Ocean fronts and their associated jets and eddies also represent a potential source of energy to drive enhanced submesoscale activity. Although submesoscales are known to be active in the Southern Ocean (*7, 8*), their structure and dynamics have not been fully characterized.

Observations. The first attempt to directly observe the three-dimensional structure of submesoscales in the Southern Ocean was made as part of the Surface MIxed Layer Evolution at Submesoscales (SMILES) project from April 18 to May 22, 2015 in a region east of Drake Passage in the Scotia Sea. During the cruise, a large northward meander of the SAF (Fig. 1a) was sampled at high resolution using towed bodies, a ship-mounted acoustic Doppler current profiler (SADCP) and surface drifters. The meander was first surveyed with 25 sections between 25 and 40 km in length made with a towed Seasoar instrument during a time when the

2

meander broke off to form an isolated mesoscale eddy (*9*). A transect through the northern edge of the meander made on May 9th, before the eddy formation process, shows two opposing fronts surrounding a cold, dense filament (Fig. 1b). The 'outer' front is associated with a very sharp temperature contrast which is partially compensated by salinity. The 'inner' front with a smaller temperature change is associated with a larger density gradient.

The cold filament and its associated fronts are embedded in a very fast current flowing clockwise around the meander. The current is nearly depth-independent over the upper 200 m. The top panel in Fig. 1b shows the velocity projected onto the direction perpendicular to the section and averaged in the upper 200 m. We will refer to this as the ACC jet. Although the ACC jet is wider than the fronts that it contains, the vertical component of the relative vorticity is large, ranging from $-0.4f$ to $0.5f$, where f is the local Coriolis frequency.

High resolution satellite imagery on May 11th indicates the presence of submesoscale meanders of the sharp temperature gradient associated with the developing meander (Fig. 1a). Qualitatively similar features have been observed before, notably along the Gulf Stream where they have been called 'shingles' and 'tongues' (*?, e.g.*)]von1955,webster. Here, the observed features have $5-15$ km wavelengths and are embedded in a broad current with speeds in excess of 1 m s^{-1}, making them difficult to observe with traditional methods due to the fast timescales associated with their advection. Immediately after completing a Seasoar survey of the newly formed eddy, we repeatedly sampled a fixed line across the fronts with the towed moving vessel profiler (MVP) (Fig. 1a). The winds were relatively weak during the Seasoar section and at the start of the MVP survey (with wind stress, $\tau < 0.1\mathrm{N/m^2}$), although the wind became strong at the end of the MVP survey ($\tau \simeq 0.25\mathrm{N/m^2}$). A timeseries of the wind stress and direction is shown in the SOM.

The MVP observations confirmed the presence of submesoscale meanders along the sharp temperature front. To visualize the approximate three-dimensional structure of the temperature

3

field, we adopt a frozen field hypothesis and convert the time of each section into an 'advected distance' by multiplying the time-elapsed since the first section by a constant velocity characteristic of the depth-averaged velocity in the mixed layer (1.2 m s^{-1}). The result, shown in Fig. 1c suggests that the meanders have a spacing of $5 - 15$ km . The meanders extend to the base of the mixed layer ($120 - 160$ m), with evidence of intrusions of cold water crossing to the warm side of the thermal front.

These observations raise a number of intriguing questions. For example, are the submesoscale meanders generated locally through an instability of the filament or fronts, and if so, what is the source of their energy? Why do the meanders appear very close to the center of the ACC jet, and how does the jet influence their formation and evolution? Do the submesoscale currents enhance subduction of surface water? We will address these questions here.

Frontal instability. To address the first of the questions listed above, we analyzed the linear stability of an idealized representation of the observed density and velocity which forms the 'basic state'. The idealized density section (black contours, Fig. 1b, lower panel) consists of two opposing fronts in a 100 m deep mixed layer. Below the mixed layer is a pycnocline with a weaker horizontal density gradient and a large vertical stratification. The velocity is taken to be in thermal wind balance with the density field, with the addition of a broad ACC jet perpendicular to the buoyancy gradient with a sinusoidal shape, a wavelength of 50 km, and a maximum velocity of 1.2 m s^{-1} (dashed line, Fig. 1b, top panel). The idealized section is assumed to be independent of the along-stream direction (parallel to the ACC jet), and curvature of the front is neglected. Further details of the idealized section are given in the SOM.

The Seasoar section (Fig. 1b) has small regions with $fq < 0$, where $q \equiv (f\hat{\mathbf{k}} + \boldsymbol{\zeta}) \cdot \nabla b$ is the potential vorticity, f is the Coriolis parameter, $\hat{k}$ is the local vertical unit vector, $\boldsymbol{\zeta} = \nabla \times \mathbf{u}$ is the relative vorticity, and b is the fluid buoyancy. As a result, conditions at the fronts are favorable for symmetric instability (*10, 11*). However, the motion associated with symmetric

4

instability is, by definition, independent of the along-front direction (*12*), and hence symmetric instability is unlikely to cause the observed meanders. To restrict our analysis to other possible instabilities, we exclude symmetric instability by adding a constant stratification to the basic state with a buoyancy frequency $N_0 = 2.5 \times 10^{-3} \text{ s}^{-1}$, which is sufficient to ensure $fq > 0$.

Despite the idealizations introduced above, the stability analysis is still complicated by the fact that the basic state is two-dimensional with variation in the cross-stream and vertical directions, rendering the equations describing the evolution of linear perturbations non-separable. To overcome this problem, we use a time-stepping method to isolate the most unstable features. The velocity and density are first decomposed into background and perturbation components:

$$\mathbf{u}(x,y,z,t) = \overline{u}(y,z)\hat{\mathbf{i}} + \mathbf{u}'(x,y,z,t), \quad \rho(x,y,z,t) = \overline{\rho}(y,z) + \rho'(x,y,z,t), \qquad (1)$$

where x, y, and z denote the along-stream, cross-stream, and vertical directions, and the overbar denotes the background state. We further decompose the perturbation variables using a Fourier transform, e.g.

$$\mathbf{u}'(x,y,z,t) = \widehat{\mathbf{u}}(k,y,z,t)e^{ikx}, \qquad (2)$$

where $\hat{}$ denotes the complex amplitude associated with along-stream wavenumber, k. Since linear perturbations evolve independently, each Fourier mode can be solved separately. We timestep the equations describing the evolution of the complex amplitude until the fastest growing instability is isolated with a constant exponential growth rate. Further details of this method are provided in the SOM.

The most unstable features develop along the outer front with an along-front wavelength of about 12.5 km (Fig. 2a). This is consistent with the observed spacing between meanders and supports the hypothesis that these features are generated through a submesoscale instability. The kinetic energy associated with the most unstable perturbations grows via the buoyancy flux (solid red line, Fig. 2a), indicative of mixed layer instability (MLI), an ageostrophic baroclinic

5

instability (*13*). The horizontal and vertical shear production remove energy from the most unstable perturbations and transfer energy to the mean flow, thereby reducing the growth rate. The negative horizontal shear production is also associated with an up-gradient flux of momentum towards the center of the ACC jet. Suppression of baroclinic instability by horizontally sheared barotropic flow has been noted before and has been termed the 'barotropic governor' (*14*). The barotropic governor is less effective at the outer front where the horizontal shear is smaller than at the inner front, explaining why the instabilities at the outer front grow faster, despite the fact that the outer front is weaker than the inner front.

The ACC jet not only influences the growth rate associated with MLI, it also controls which front is the most unstable. To show this, we repeated the linear stability analysis without the ACC jet included in the basic state. When the ACC jet is removed, the growth rate associated with the fastest growing mode increases by a factor of 2.3 as the vertical shear production becomes a significant source (Fig. 2a). Remarkably, without the ACC jet, the most unstable mode shifts from the outer front to the inner front where the horizontal density gradient is larger (Fig. 2b).

Nonlinear evolution. To examine the nonlinear evolution of the submesoscale instabilities and their influence on the evolution of the fronts, we used fully nonlinear, nonhydrostatic numerical simulations starting with the same idealized initial conditions described above. The model domain was 50 km in both horizontal directions and 200 m in the vertical direction. The flow is uniform in the along-stream (x) direction. The simulations use free-slip, adiabatic, rigid lid boundary conditions at the top and bottom of the domain and are therefore unforced by wind or surface heating/cooling. Gridpoints were uniformly spaced with a resolution of about 100 m in the horizontal directions and 1 m in the vertical. Unresolved motions were parameterized with constant Laplacian viscosity and diffusivity with coefficients of $0.3 \ \mathrm{m^2 \ s^{-1}}$ and $3 \times 10^{-5} \ \mathrm{m^2 \ s^{-1}}$ in the horizontal and vertical directions, respectively. Growing modes are seeded using random

perturbations with an amplitude of 1 mm s^{-1}.

As in the linear stability analysis, we ran simulations with and without the ACC jet. Without the ACC jet, a submesoscale instability first develops along the inner front with an along-stream wavelength of about 12.5 km, consistent with the location and scale of the most unstable mode predicted from the linear stability analysis. After about 10 days of simulation time, four distinct cyclonic submesoscale eddies develop. These eddies interact with each other and eventually fill the domain with a field of submesoscale fronts and eddies (Fig. 3a, upper left inset).

The nonlinear evolution of the submesoscale instabilities is dramatically different in the presence of the ACC jet. Here, a submesoscale instability first develops along the outer front. As the submesoscale wave develops, it rolls up into a billow-like structure (Fig. 3a, upper right inset) before an instability develops on the inner front. Later, the submesoscales interact nonlinearly and lead to a state with temperature filaments and eddies on a broader range of scales (Fig. 3a, lower right inset). Remarkably, the zonal frontal structure remains intact in this case.

The relative distortion of the temperature front can be quantified by calculating the equivalent contour length,

$$L_{eq}(T,t) = \left[\frac{\frac{\partial}{\partial A} \int \int |\nabla_h T|^2 dA}{(\partial T/\partial A)^2} \right]^{1/2}, \tag{3}$$

where $A(T, t)$ is the horizontal surface area occupied by water with temperature less than T and ∇_h is the horizontal gradient operator (*15, 16*). Here, we define $\overline{L}_{eq}$ as the average of L_{eq} over the temperature range $3°C \leq T \leq 4.5°C$ and compare this with $\overline{L}_0$, the value of $\overline{L}_{eq}$ associated with the initial conditions. In both simulations, $\overline{L}_{eq}$ increases as submesoscale instabilities develop and distort the temperature contours, and in both cases the growth of $\overline{L}_{eq}$ saturates after $25 - 30$ days (*?*) (note, the long spinup time is partly due to the small amplitude of the disturbances used to initialize the models.) When the ACC jet is present $\overline{L}_{eq} < 5L_0$, significantly smaller than in the simulation without the ACC jet (Fig. 3a). For comparison,

7

when normalized by the length of an undisturbed temperature contour, the MVP observations give $\overline{L}_{eq} \simeq 1.5\overline{L}_0$. This is somewhat smaller but generally within one standard deviation of the prediction from the model with a jet when sub-sampled at the approximate resolution of the observations. In contrast, without an ACC jet, the saturated value of $\overline{L}_{eq}$ is more than 20 times larger than L_0.

Submesoscale Rossby waves. The ACC jet transforms the developing instabilities into submesoscale Rossby waves. Upstream phase propagation is evident in the model at the center of the outer front (Fig. 3b). The phase propagation is consistent with Rossby waves supported by the local gradient of potential vorticity. Although the velocity and density in the model are non-trivial functions of depth and cross-stream distance, a simple dispersion relation for quasi-geostrophic (QG) Rossby waves can be written by assuming that stratification is constant in the mixed layer, the mixed layer base is rigid, and the Rossby nubmer is small:

$$\omega = kc_p = \overline{u}k + \frac{-\beta + \overline{u}_{yy}}{|\mathbf{k}|^2 + \frac{n^2\pi^2}{R_{ML}^2}}, \tag{4}$$

where ω and c_p are the frequency and phase velocity, n is the vertical mode number, $R_{ML} = N_{ML}H_{ML}/f_0$ is the mixed layer deformation radius, and N_{ML} and H_{ML} are the buoyancy frequency and depth associated with the mixed layer. The power spectrum of the cross-stream velocity, calculated along the center of the front, shows distinct peaks coinciding with the dispersion relation for barotropic ($n = 0$) and mode 1 mixed layer baroclinic ($n = 1$) Rossby waves. Note that dispersion curves for deeper baroclinic modes with penetration into the thermocline lie between the indicated lines.

Downwelling. Comparing the horizontal slices of temperature at 50-m depth from the model with an ACC jet, it is evident that the water associated with the cold filament (defined by temperatures $< 1.5°C$) occupies less horizontal surface area after 60 days of model time than at 30 days or the initial state (Fig. 3a, right insets). The observations also suggest active

subduction of the filament water. Comparing the Seasoar section (Fig. 1b) with a composite of the later MVP sections (Fig. 4a) reveals that the filament water which was seen at the surface in the Seasoar section is only seen near the base of the mixed layer in the MVP survey. An along-stream average of the temperature from the model reproduces the slumping of the cold filament (compare Figs. 4a and 4b) which then spreads out at the base of the mixed layer. Note that the very cold water appearing in the bottom left of Fig. 4a was not included in the model initial conditions where temperature was initially depth-independent with a minimum value of about 1.2 $^\circ C$. In the model, the water that began in the filament forms periodic intrusions of cold water on the warm side of the outer front, qualitatively similar to those seen in Fig. 1c. Because the initial condition was in thermal wind balance and the model does not include surface forcing or mesoscale eddies, subduction in the model can be directly linked to submesoscale activity.

In the later stages of the model simulation, the submesoscale Rossby waves are associated with intense vertical circulations. The *rms* vertical velocity and mean density, calculated using an along-stream (x) average at a depth of 50 m, are shown in Fig. 5a and 5b. In the model without the ACC jet (Fig. 5a), the *rms* vertical velocity reaches a maximum value of approximately 50 m day^{-1} as instabilities develop at the inner front, a value consistent with previous models of submesoscale flows (*17–19*). When the ACC jet is included in the model the *rms* vertical velocity is significantly larger (approximately 100 m day^{-1}) and large *rms* vertical velocities are maintained until the end of the simulation. The simulation also exhibits a strong internal gravity wave field which leads to large *rms* vertical velocities on the flanks of the jet.

The submesoscale instabilities drive subduction of the cold, dense filament initially found between the inner and outer fronts. The total volume of water with potential density $\sigma_\theta >$ 26.95 kg m^{-3} passing through a horizontal plane at 50-m depth is similar for both simulations (Fig. 5c), although with the ACC jet the rate of subduction is weaker ($\simeq 6,500$ m^3/s) but

more sustained than in the absence of the ACC jet. Subduction eventually ends once the dense filament sinks to the base of the mixed layer (Fig. 4), which is a consequence of the unforced simulations in a periodic horizontal domain. In reality, re-supply of dense water to the filament or vertical mixing in response to intermittent storm events could sustain subduction. Note that the subduction rate decreases by about a factor of 10 if we exclude the 'inner' front from the model initial conditions (see SOM), although the qualitative features of the simulations with and without ACC jets remain very similar.

Implications. The results presented here indicate that the strong currents associated with the ACC confine submesoscales to a localized region near the core of the ACC jet and support submesoscale Rossby waves. In the absence of wind, surface cooling, or large scale confluence, net subduction of water in a dense filament occurs during the development of submesoscale instabilities. Following the equilibration of submesoscale instabilities and development of submesoscale Rossby waves, the net subduction rate slows but large localized vertical velocities persist near the center of the ACC jet (Fig. 5b,c).

To put the model subduction rate in context, we can attempt to extrapolate the simulation results to the full ACC. The dense filament where subduction was observed occupied the potential density class $\sigma_\theta = 26.95 - 27.01$ kg m^{-3}. Using the methodology described in (*4*), the total subduction induced by mesoscale and larger scale motion in this density class within the Southern Ocean is 2.9 Sv. Based on climatological frontal position (*20*) and mixed layer temperature and salinity (*21*), this density range outcrops along 6787 km of the Polar Front (PF) and 2381 km of the Subantarctic Front (SAF). Our simulations indicate a subduction rate of about 6.5×10^{-3} Sv integrated over the 50-km long dense filament. If the same subduction rate occurs across the full length of the PF and SAF, these estimates would imply 0.9 Sv of subduction at the PF and 0.3 Sv of subduction at the SAF within the same density class. This estimate implies that submesoscales can induce 1.2 Sv of subduction in this density class, a significant rate compared

to the 2.9 Sv subducted by larger scale motions.

The estimates above were based on the observed density section (Fig. 1b) with two fronts surrounding a dense filament. Removing one of these fronts from the initial condition and keeping the 'outer' front with a smaller potential density change of 0.05 kg/m^3 reduces the subduction rate by about a factor of 10 (see SOM). The strength and structure of the ACC fronts varies in space and time (*22*). There might also be significant seasonal variability in the submesoscale activity (*23, 24*) which is not taken into account in this estimate. Additional observations or numerical simulations could help to better quantify the influence of submesoscales on subduction along the ACC.

Persistent subduction of water in a specific density class would require a mechanism to re-supply water in this density class to fronts or filaments along the ACC. Our simulations do not show a significant change in the volume associated with each density class (see SOM), suggesting that another process is needed. Net advection of dense surface water towards the front or water mass transformation are two candidates. Our simulations exclude net advection towards the front due to the periodic boundary conditions. Wind and air-sea heat fluxes are likely important factors in contributing to water mass transformation, and both of these processes were excluded from the simulations.

The subduction of mode water, which occurs north of the SAF in the Scotia Sea (*4, 25*), is intimately linked to the Southern Ocean sink of anthropogenic heat and carbon (*5, 6, 26*). Although our observations were limited in time and space, high-resolution numerical models could help to quantify the influence of submesoscales on water mass subduction along the ACC fronts. Submesoscale processes are not presently resolved in climate models and quantifying their associated subduction rates has the potential to improve estimates of the ocean uptake of heat and carbon.

The fronts associated with the ACC are known to act as barriers to lateral mixing (*27, 28*),

11

although much of the past work in this area has not directly considered the influence of submesoscales. Here, we find that the ACC jet restricts submesoscale activity to the center of the front and supports submesoscale Rossby waves, and the front is much less distorted by submesoscales than it would be if the jet were absent. The large reduction in equivalent temperature contour length (Fig. 3a) implies a strong reduction in the effective horizontal diffusivity associated with stirring by submesoscale motions (*29*). Regional variations in the confinement of submesoscales at ACC fronts could modulate lateral mixing rates in the Southern Ocean. This could have important implications for the exchange of surface waters between the Southern Ocean and the surrounding ocean basins.

Submesoscales have been shown to enhance primary production by upwelling nutrient-rich water into the euphotic layer (*3,30*) and reducing light limitation (*31–33*). Although chlorophyll concentrations in the Southern Ocean are generally low, elevated concentrations have been observed near major fronts (*34*). The influence of submesoscale physics on primary production in the Southern Ocean is not well understood, but future observational campaigns and modeling studies could help quantify this influence. In particular, the very large vertical velocities reported here (Fig. 5b) could stimulate primary production along the front by bringing nutrients up into the euphotic layer (*35*).

One of the remarkable features of the simulation with a strong ACC jet is the coherence of the front at the end of the model simulation. The linear stability analysis shows that the ACC jet reduces the growth rate of submesoscale instabilities, but it does not fully stabilize the flow. The mechanisms behind the jet-induced equilibration of the front remain unknown. Building a dynamical description of this process will be important to predicting properties of the fully-developed system including the frontal width and the size of the submesoscale eddies. This will also be an important step in extrapolating the results presented here to other regions of the global ocean.

Materials and Methods

Numerical Simulations: The numerical simulations use a code developed and described in (*36*). The code solves the non-hydrostatic, incompressible, Boussinesq equations. The numerical method combines a pseudo-spectral method in both horizontal directions with a second-order accurate centered finite difference method in the vertical direction. The timestepping algorithm uses a mixed third-order accurate Runge-Kutta scheme and Crank-Nicolson for the viscous/diffusive terms. The non-hydrostatic pressure is treated using the projection method of (*37*). The $2/3$ de-aliasing method (*38*) is used to prevent spurious aliasing associated with the Fourier transform applied to the nonlinear advection terms. The initial conditions are described in detail in the Supplementary Material.

Linear stability analysis: The linear stability analysis reported in Figure 2 was performed by time-stepping the linearized governing equations. A two-dimensional basic state was first prescribed using the initial conditions described in the Supplementary Material. The basic state varies only in the cross-front (y) and vertical (z) directions. All fields are decomposed into departures from the basic state, e.g. $u = \overline{u}(y,z) + u'(x,y,z,t)$. The equations for departures from the basic state (e.g. u') were then linearized, assuming small departures from the basic state (e.g. $u' << \overline{u}$). A Fourier transform was then applied in the along-front (x) direction to yield a set of equations for the complex Fourier amplitudes (e.g. $\hat{u}(k,y,z,t)$). A set of discrete along-front wavenumbers (k) was chosen. For each wavenumber, the linearized equations for the Fourier amplitudes was time-stepped until the exponential growth (or decay) rate reaches a steady state. At the start of each time-stepping loop, the Fourier amplitudes were seeded with a set of random perturbations with uniform amplitude in Fourier space.

The numerical method used in the linear stability solver is similar to that used in the fully nonlinear simulations, except that second order centered finite differences are used to calculate derivatives in the y and z directions. The time-stepping method uses the same third-order ac-

curate Runge-Kutta / Crank Nicolson method as in the nonlinear simulations and the projection method is used to calculate the non-hydrostatic pressure.

References and Notes

1. J. Marshall, K. Speer, Closure of the meridional overturning circulation through southern ocean upwelling. *Nature Geoscience* **5**, 171–180 (2012).

2. L. N. Thomas, A. Tandon, A. Mahadevan, Submesoscale processes and dynamics. *Ocean modeling in an Eddying Regime* pp. 17–38 (2008).

3. M. Lévy, R. Ferrari, P. J. Franks, A. P. Martin, P. Rivière, Bringing physics to life at the submesoscale. *Geophysical Research Letters* **39** (2012).

4. J.-B. Sallée, K. Speer, S. Rintoul, S. Wijffels, Southern ocean thermocline ventilation. *Journal of Physical Oceanography* **40**, 509–529 (2010).

5. T. L. Frölicher, J. L. Sarmiento, D. J. Paynter, J. P. Dunne, J. P. Krasting, M. Winton, Dominance of the southern ocean in anthropogenic carbon and heat uptake in cmip5 models. *Journal of Climate* **28**, 862–886 (2015).

6. S. Khatiwala, F. Primeau, T. Hall, Reconstruction of the history of anthropogenic co2 concentrations in the ocean. *Nature* **462**, 346–349 (2009).

7. I. Rosso, A. M. Hogg, A. E. Kiss, B. Gayen, Topographic influence on submesoscale dynamics in the southern ocean. *Geophysical Research Letters* **42**, 1139–1147 (2015).

8. C. B. Rocha, T. K. Chereskin, S. T. Gille, D. Menemenlis, Mesoscale to submesoscale wavenumber spectra in drake passage. *Journal of Physical Oceanography* **46**, 601–620 (2016).

9. K. A. Adams, P. Hosegood, J. R. Taylor, J.-B. Sallée, S. Bachman, R. Torres, M. Stamper, Frontal circulation and submesoscale variability during the formation of a southern ocean mesoscale eddy. *Journal of Physical Oceanography* **47**, 1737–1753 (2017).

10. D. Bennetts, B. Hoskins, Conditional symmetric instability-a possible explanation for frontal rainbands. *Quarterly Journal of the Royal Meteorological Society* **105**, 945–962 (1979).

11. J. R. Taylor, R. Ferrari, On the equilibration of a symmetrically unstable front via a secondary shear instability. *Journal of Fluid Mechanics* **622**, 103–113 (2009).

12. P. H. Stone, On non-geostrophic baroclinic stability. *Journal of the Atmospheric Sciences* **23**, 390–400 (1966).

13. G. Boccaletti, R. Ferrari, B. Fox-Kemper, Mixed layer instabilities and restratification. *Journal of Physical Oceanography* **37**, 2228–2250 (2007).

14. I. James, L. Gray, Concerning the effect of surface drag on the circulation of a baroclinic planetary atmosphere. *Quarterly Journal of the Royal Meteorological Society* **112**, 1231–1250 (1986).

15. N. Nakamura, Two-dimensional mixing, edge formation, and permeability diagnosed in an area coordinate. *Journal of the atmospheric sciences* **53**, 1524–1537 (1996).

16. J. Marshall, E. Shuckburgh, H. Jones, C. Hill, Estimates and implications of surface eddy diffusivity in the southern ocean derived from tracer transport. *Journal of physical oceanography* **36**, 1806–1821 (2006).

17. A. Mahadevan, A. Tandon, An analysis of mechanisms for submesoscale vertical motion at ocean fronts. *Ocean Modelling* **14**, 241–256 (2006).

18. X. Capet, J. C. McWilliams, M. J. Molemaker, A. Shchepetkin, Mesoscale to submesoscale transition in the california current system. part i: Flow structure, eddy flux, and observational tests. *Journal of Physical Oceanography* **38**, 29–43 (2008).

19. L. Brannigan, Intense submesoscale upwelling in anticyclonic eddies. *Geophysical Research Letters* **43**, 3360–3369 (2016).

20. J. Sallée, K. Speer, R. Morrow, Response of the antarctic circumpolar current to atmospheric variability. *Journal of Climate* **21**, 3020–3039 (2008).

21. V. Pellichero, J.-B. Sallée, S. Schmidtko, F. Roquet, J.-B. Charrassin, The ocean mixed-layer under southern ocean sea-ice: Seasonal cycle and forcing. *Journal of Geophysical Research: Oceans* (2016).

22. S. Sokolov, S. R. Rintoul, Circumpolar structure and distribution of the antarctic circumpolar current fronts: 2. variability and relationship to sea surface height. *Journal of Geophysical Research: Oceans* **114** (2009).

23. J. Callies, G. Flierl, R. Ferrari, B. Fox-Kemper, The role of mixed-layer instabilities in submesoscale turbulence. *Journal of Fluid Mechanics* **788**, 5–41 (2016).

24. A. F. Thompson, A. Lazar, C. Buckingham, A. C. Naveira Garabato, G. M. Damerell, K. J. Heywood, Open-ocean submesoscale motions: A full seasonal cycle of mixed layer instabilities from gliders. *Journal of Physical Oceanography* **46**, 1285–1307 (2016).

25. I. Cerovečki, L. D. Talley, M. R. Mazloff, G. Maze, Subantarctic mode water formation, destruction, and export in the eddy-permitting southern ocean state estimate. *Journal of physical oceanography* **43**, 1485–1511 (2013).

26. J.-B. Sallée, R. J. Matear, S. R. Rintoul, A. Lenton, Localized subduction of anthropogenic carbon dioxide in the southern hemisphere oceans. *Nature Geoscience* **5**, 579–584 (2012).

27. A. C. Naveira Garabato, R. Ferrari, K. L. Polzin, Eddy stirring in the southern ocean. *Journal of Geophysical Research: Oceans* **116** (2011).

28. E. Shuckburgh, H. Jones, J. Marshall, C. Hill, Understanding the regional variability of eddy diffusivity in the pacific sector of the southern ocean. *Journal of Physical Oceanography* **39**, 2011–2023 (2009).

29. R. Abernathey, J. Marshall, M. Mazloff, E. Shuckburgh, Enhancement of mesoscale eddy stirring at steering levels in the southern ocean. *Journal of Physical Oceanography* **40**, 170–184 (2010).

30. A. Mahadevan, The impact of submesoscale physics on primary productivity of plankton. *Annual review of marine science* **8**, 161–184 (2016).

31. J. R. Taylor, R. Ferrari, Ocean fronts trigger high latitude phytoplankton blooms. *Geophysical Research Letters* **38** (2011).

32. A. Mahadevan, E. DAsaro, C. Lee, M. J. Perry, Eddy-driven stratification initiates north atlantic spring phytoplankton blooms. *Science* **337**, 54–58 (2012).

33. J. Taylor, Turbulent mixing, restratification, and phytoplankton growth at a submesoscale eddy. *Geophysical Research Letters* **43**, 5784–5792 (2016).

34. J. K. Moore, M. R. Abbott, Phytoplankton chlorophyll distributions and primary production in the southern ocean. *Journal of Geophysical research* **105** (2000).

35. T. N. Lee, J. A. Yoder, L. P. Atkinson, Gulf Stream frontal eddy influence on productivity of the southeast us continental shelf. *Journal of Geophysical Research: Oceans* **96**, 22191–22205 (1991).

36. J. R. Taylor, *Numerical simulations of the stratified oceanic bottom boundary layer* (University of California, San Diego, 2008).

37. G. E. Karniadakis, M. Israeli, S. A. Orszag, High-order splitting methods for the incompressible navier-stokes equations. *Journal of computational physics* **97**, 414–443 (1991).

38. S. A. Orszag, Numerical simulation of incompressible flows within simple boundaries. i. galerkin (spectral) representations. *Studies in applied mathematics* **50**, 293–327 (1971).
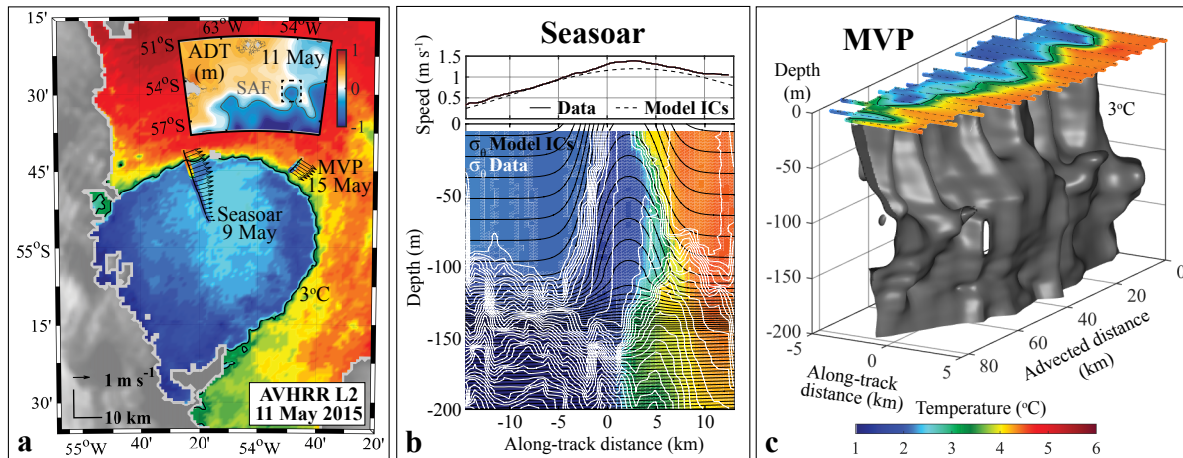
18

Figure 1: (a) Map of survey site with temperature (color, main panel) and dynamic topography (ADT), and locations of the Seasoar section and MVP survey with surface temperature (colored dots) and surface velocity vectors. (b) Seasoar section from 9 May with depth-averaged along-front current speed (top) and temperature and potential density (bottom panel, color shading and white contours). The corresponding model initial conditions (model ICs) are also shown. The potential density contour interval is 0.01 kg m^{-1}. (c) MVP survey conducted on 15 May at the location indicated in panel (a). The time of each section is converted to 'advected distance' by multiplying the approximate speed of the ACC jet (1.2 m/s). The top surface shows temperature from the MVP, averaged above 20 m depth (shading), and from the ship's flow through intake (colored dots). The 3° C isotherm is interpolated into along-track, advected distance, and depth coordinates and displayed as a gray isosurface.

39. W. Large, S. Pond, Open ocean momentum flux measurements in moderate to strong winds.
    Journal of physical oceanography **11**, 324–336 (1981).

40. J. R. Taylor, R. Ferrari, Buoyancy and wind-driven convection at mixed layer density fronts.
    Journal of Physical Oceanography **40**, 1222–1242 (2010).

41. L. N. Thomas, J. R. Taylor, R. Ferrari, T. M. Joyce, Symmetric instability in the gulf stream.
    Deep Sea Research Part II: Topical Studies in Oceanography **91**, 96–110 (2013).

42. J. C. McWilliams, *Proc. R. Soc. A* (The Royal Society, 2016), vol. 472, p. 20160117.
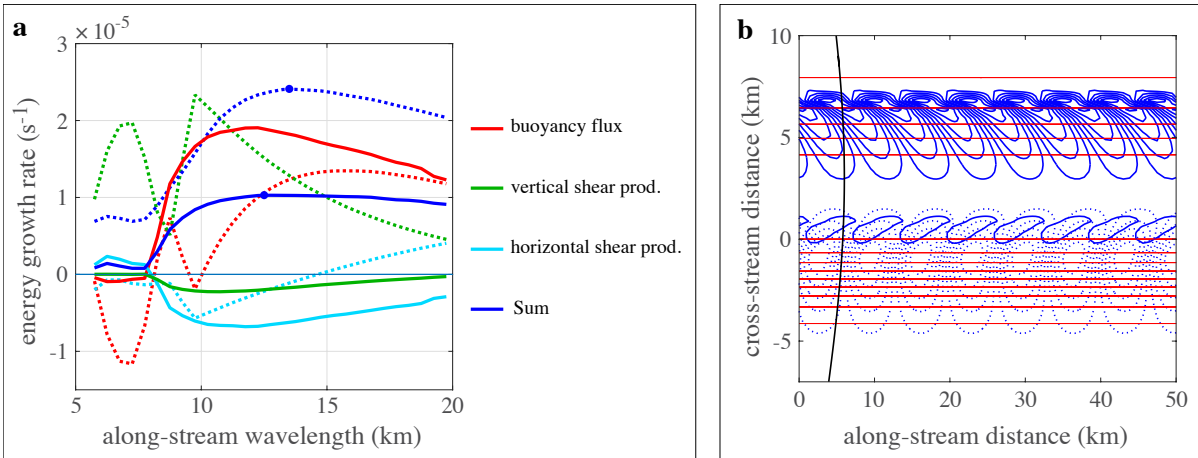
Figure 2: Linear stability analysis of the model initial conditions shown in Fig. 1b. (a) Perturbation energy source terms for a basic state with (solid) and without (dotted) the ACC jet. Blue dots indicate the most unstable mode. (b) Density perturbations associated with the most unstable mode with (solid blue) and without (dotted blue) the ACC jet. Surface density contours (red) and the ACC jet profile (black) are also shown.
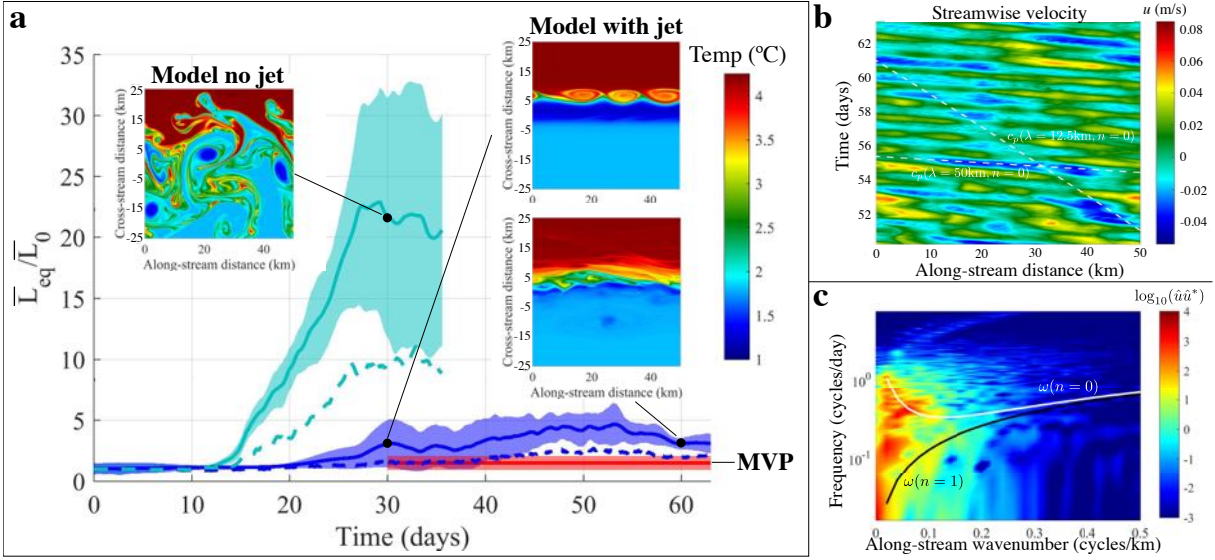
Figure 3: (a) Equivalent temperature contour length, L_{eq}, as defined in Eq. 3, normalized by its minimum value, L_0, and averaged from $3 - 4.5°C$ (solid lines). Shaded regions indicate $\pm$ one standard deviation about the average over the temperature range. Dashed lines indicate the mean value of L_{eq} from each model, subsampled (with 4 km x 400 m resolution) to approximate the spacing of the MVP measurements. Insets show the temperature at a depth of 50 m. (b) Space-time diagram of the streamwise velocity at 50 m depth and a cross-stream distance of 4.25 km for the late stages of the model simulation with a jet included. Note that the velocity associated with the ACC jet at this location has been subtracted from u. White dashed lines have a slope equal to the phase speed calculated from Eq. (4) with the indicated along-stream wavelengths and independent of the cross-stream direction. (c) Power spectrum associated with the along-stream velocity at the same cross-stream distance as in panel (b), calculated for the full duration of the model with an ACC jet. Solid white and black lines indicate the dispersion relation from Eq. (4) for mixed layer baroclinic modes ($n = 1$) and barotropic modes ($n = 0$). In both cases, the cross-stream wavenumber is set to zero.
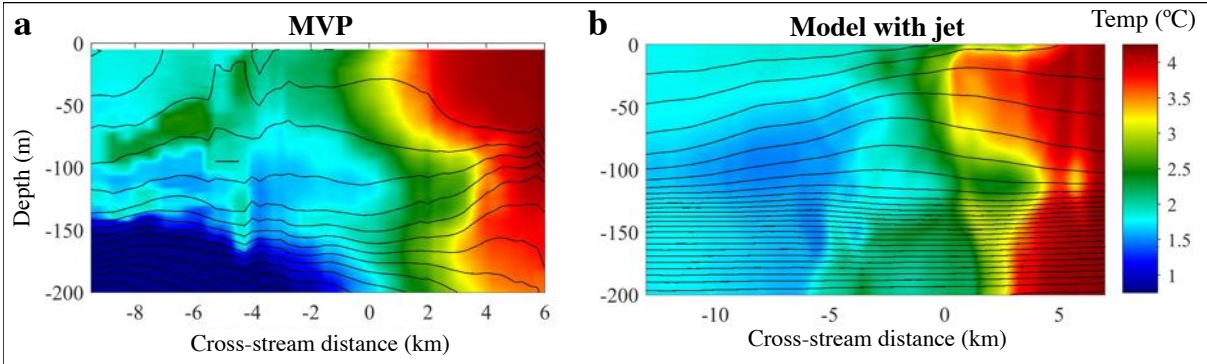
Figure 4: (a) Composite temperature (color) and density (black contours), averaged for all MVP sections. (b) Along-stream (x) averaged temperature (color) and density (black contours) from the Model with the ACC jet at 53 days. The initial temperature was independent of depth in the model.
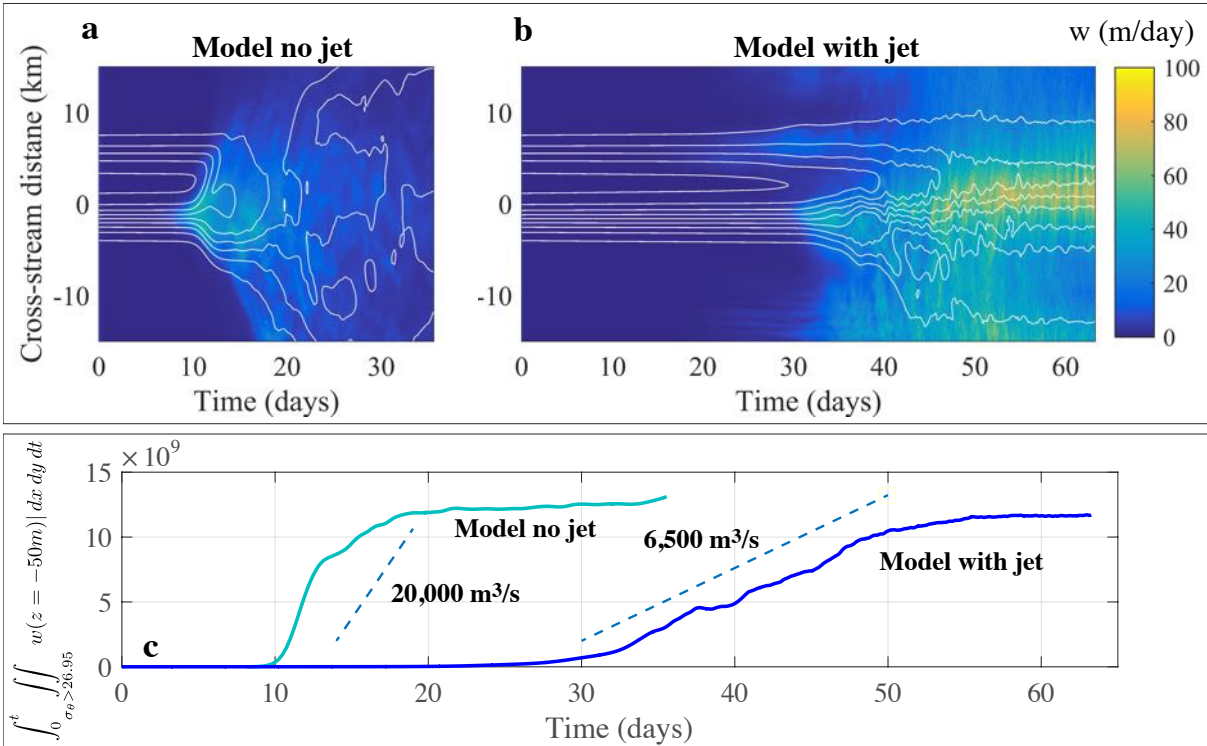

Figure 5: rms vertical velocity at $z = 50$ m depth with respect to an average in the x direction, from the model without (a) and with (b) the ACC jet. White contour lines show x-averaged density with a contour interval of 0.01 kg m^{-1}. Volume of water with potential density $\sigma_\theta > 26.95$kg/m^3 subducted below $z = -50$m. The slope of the dashed lines corresponds to the labeled volumetric subduction rate.

22

Supplementary Materials
Submesoscale Rossby Waves on the Antarctic Circumpolar Current

John R. Taylor,[1]* Scott Bachman,[1] Megan Stamper,[1] Phil Hosegood[2],
Katherine Adams[2], Jean-Baptiste Sallee[3], Ricardo Torres[4]

[1]Department of Applied Mathematics and Theoretical Physics, University of Cambridge,
Centre for Mathematical Sciences, Wilberforce Road, Cambridge, UK, CB3 0WA.

[2]School of Marine Science and Engineering, Plymouth University

[3]Sorbonne Universites, UPMC/CNRS, LOCEAN Laboratory

[3]Plymouth Marine Laboratory

*To whom correspondence should be addressed; E-mail: J.R.Taylor@damtp.cam.ac.uk.

1 Observations

Two different towed CTD (conductivity, temperature and depth) bodies were used for hydrographic data collection during the SMILES research cruise aboard the RRS James Clark Ross. The Seasoar collected data from the surface to 200-m water depth in a to-yo pattern with a Seabird Electronics, Inc. SBE49 FastCAT CTD sensor which sampled at 16 Hz. With a tow speed of 8 knots (4.1 m s^{-1}), the maximum horizontal spacing between dives is 200 m.

The Moving Vessel Profiler (MVP) also collected data at 25 Hz with an AML Oceanographic 7027 CTD. Towed at 4 knots (2.1 ms^{-1}), the MVP free-falls to a depth of 300 m and is winched back up to the surface. The horizontal separation of a dive-climb cycle is approximately 1 km. A temperature-conductivity cell lag correction of 4 ms is applied to the measured temperature data.
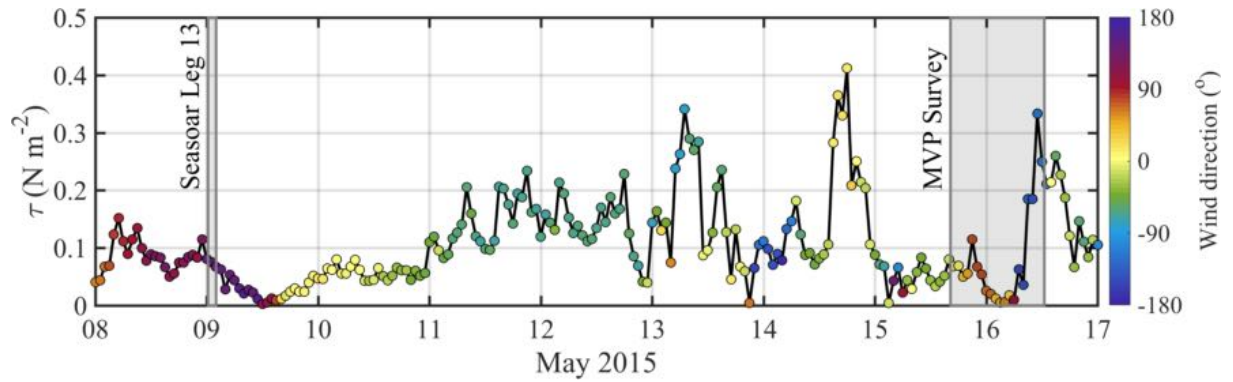
Figure S1: Wind stress (N/m^2) and wind angle (degrees from east) calculated using the algorithm from Large et al. , 1981.

An Ocean Science 75 kHz acoustic Doppler current profiler (ADCP) collected horizontal velocities in 8-m depth bins. Data from 30-m to the depth of the towed CTDs are used in this paper (200 m Seasoar, 300 m MVP).

The CTD and ADCP data processing, detailed in Adams et al., 2017, produced datasets on a 0.5 km by 2 m regularly-spaced grid. Potential density anomaly (kg m^{-3}) is calculated for both CTD datasets using ITS90 referenced to the surface.

Thermosalinograph, or underway Oceanlogger CTD, data was collected at the ships intake located at approximately 4-m depth. The recorded Oceanlogger data had a temporal resolution of 3 to 5 s. The underway temperature data (Figure 1b) is interpolated to regular 10-s intervals which yields a horizontal resolution of 20 m during the MVP survey.

A timeseries of the wind stress and direction is shown in Figure S1 along with the duration of the Seasoar section (Seasoar Leg 13) and MVP surveys shown in Figure 1 of the main text. The wind stress was calculated using the algorithm described in Large et al. , 1981. The winds were relatively weak during the Seasoar section and at the start of the MVP survey. The wind stress became larger ($\tau > 0.2N/m^2$) at the end of the MVP survey.

2 Numerical simulations

The computational domain is 50km in each horizontal directions and 200m in the vertical direction. A uniform grid with 512 gridpoints is used in each horizontal direction and 121 gridpoints are used in the vertical direction with higher resolution near both boundaries. The maximum vertical grid spacing is 2.1m and the minimum vertical grid spacing is 1.0m.

Periodic boundary conditions are applied to all variables in the horizontal direction. Since the density and temperature fields are not periodic in the y-direction, a constant background gradient is subtracted from both fields such that departures from this background gradient are periodic. This technique has been used in several previous studies (e.g. Taylor and Ferrari, 2010, Thomas et al. 2013). This method effectively preserves the density and temperature difference across the domain in the y-direction.

Free-slip (no-stress) boundary conditions are applied to the horizontal velocity at the top and bottom of the computational domain. The vertical velocity is set to zero at both boundaries. A no flux condition is applied to density and temperature at the upper boundary, and at the lower boundary the density and temperature gradient match their initial values (see initial conditions below).

The horizontal and vertical viscosity and diffusivity in the model were set to $\kappa_h = \nu_h = 0.3$ m^2 s^{-1} and $\kappa_v = \nu_v = 3 \times 10^{-5}$ m^2 s^{-1}. These values were determined by fixing the ratio of the horizontal and vertical components based on the squared ratio of the horizontal and vertical grid spacing, i.e.

$$\frac{\kappa_h}{\kappa_v} = \left(\frac{\Delta x}{\Delta z}\right)^2. \tag{1}$$

The coefficient of diffusion was then adjusted to give the smallest value possible without allowing buildup of spurious grid-scale noise.

3 Model initial conditions

Here, we describe the initial conditions used for the linear stability analysis and nonlinear numerical simulations. Since we use a linear equation of state, we describe the density in terms of a single dynamical variable, in this case the fluid buoyancy ($b \equiv -g\rho/\rho_0$). The initial buoyancy is prescribed by first defining three distinct vertical layers, the mixed layer for $z > -100$m, the transition layer for -140m $< z < -100$m, and the thermocline for -200m $< z < -140m$, where z is the distance from the ocean surface (with $+z$ upward). The variation in buoyancy in the cross-front (y) direction is taken to be independent of depth:

$$
\begin{aligned}
b(y) = & \left(-4.5 \times 10^{-4}\tfrac{\text{m}}{\text{s}^2}\right) \left(\tanh((y - LY/2 + 1.74\text{km})/2\text{km}) + 1\right) \\
& + \left(2.5 \times 10^{-4}\tfrac{\text{m}}{\text{s}^2}\right) \left(\tanh((y - LY/2 - 5.5\text{km})/2\text{km}) + 1\right).
\end{aligned}
$$

where $LY/2$ is the center of the domain in the spanwise direction. The vertical stratification varies in each layer with a constant vertical buoyancy gradient in the mixed layer and thermocline:

$$
\begin{aligned}
N^2_{\text{ML}} &= 6.5 \times 10^{-6}\text{s}^{-2} \\
N^2_{\text{thermocline}} &= 4 \times 10^{-5}\text{s}^{-2}.
\end{aligned}
$$

The stratification in the transition layer is set by linearly interpolating between the buoyancy at the top of the thermocline and the bottom of the mixed layer, where the mixed layer buoyancy is offset by an additional $+1.25 \times 10^{-3}\text{ms}^{-2}$.

Temperature was treated in the model as a passive scalar, consistent with the assumption of a linear equation of state. For simplicity, the initial temperature was assumed to be independent
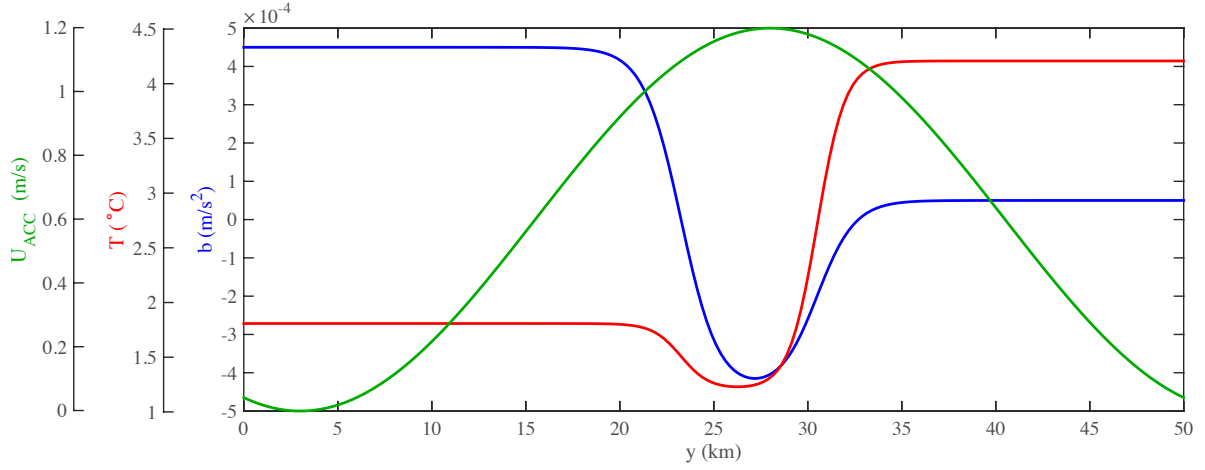
Figure S2: Profiles of the buoyancy (blue), temperature (red), and depth-averaged velocity (green) associated with the model initial conditions (model ICs) and the linear stability analysis.

of depth and along-front distance. Specifically, the initial temperature field was:

$$T(y) = (3°C) \quad - (0.3°C) \left(\tanh((y - LY/2 + 1.74\text{km})/1.5\text{km})\right)$$
$$+ (1.5°C) \left(\tanh((y - LY/2 - 5.5\text{km})/1.5\text{km})\right).$$

The initial velocity field included a component in thermal wind balance with the buoyancy field. The reference level (where the thermal wind velocity is zero) was taken to be the middle of the mixed layer ($z = -50m$). In addition, in some simulations an additional depth-independent 'ACC jet' is added to the initial velocity field with the form:

$$U_{ACC} = \left(0.6\text{ms}^{-1}\right) \cos \left(\frac{2\pi}{LY}(y - LY/2 - 3\text{km})\right) + 0.6\text{ms}^{-1}.$$

In order to ease the CFL constraint on the timestep, the numerical simulations were done in a reference frame moving in the $+x$ direction with half of the maximum jet speed. Cross-front profiles of the buoyancy, temperature, and ACC jet are shown in Figure S3.

4 Subduction estimate

The subduction rate from the simulation is extrapolated to the ACC for the density class of the dense filament (26.95 kg m^{-3} $< \sigma_\theta < 27.01$ kg m^{-3}). Circumpolar climatological positions of the SAF and PF, based on altimetry (Sallee et al. 2008), are used here to approximate the frontal locations. Incremental frontal lengths (distance between two adjacent frontal positions) are compared with a mixed layer density climatology (Pellichero et al. 2016). Cumulative frontal lengths are computed for each front as the cumulative sum of incremental frontal lengths that are located within the specified density class (see Fig. 1). The resulting cumulative frontal length of the SAF (PF) is 2381 km (6787 km). A subduction estimate for the ACC is estimated by applying these cumulative frontal lengths to the horizontal subduction rate from the simulation (6.5×10^{-3} Sv / 50 km = 0.13 m^2/s). This yields the reported submesoscale-driven subduction values of 0.9 Sv (PF) and 0.2 Sv (SAF), or 1.1 Sv in total.

For comparison, we also calculate a larger-scale subduction estimate for the same density class. The annual average subduction analysis from Sallee et al. 2010 (Fig. 10) is applied to the filament density class and yields a circumpolar estimate of 2.9 Sv. Processes considered in this estimate include Ekman, lateral induction and eddy-induced subduction.

Subduction in the model is largely adiabatic. Figure **??** shows probability density functions (PDFs) of the potential density σ_θ for each simulation. For reference, the PDF at $t = 10$ days is also shown, before submesoscale instabilities develop. Here, we chose $t = 10$ days instead of the initial condition at $t = 0$ because weak diffusion in the first 10 days reduces noise in the PDF due to jumps in density associated with the model grid. The shape of the PDF at $t = 0$ and $t = 10$ days are not significantly different. There is very little change in the PDFs at the end of each simulation, indicating that the water parcels approximately maintain their original density.

The initial conditions in the model consisted of two opposing fronts surrounding a dense
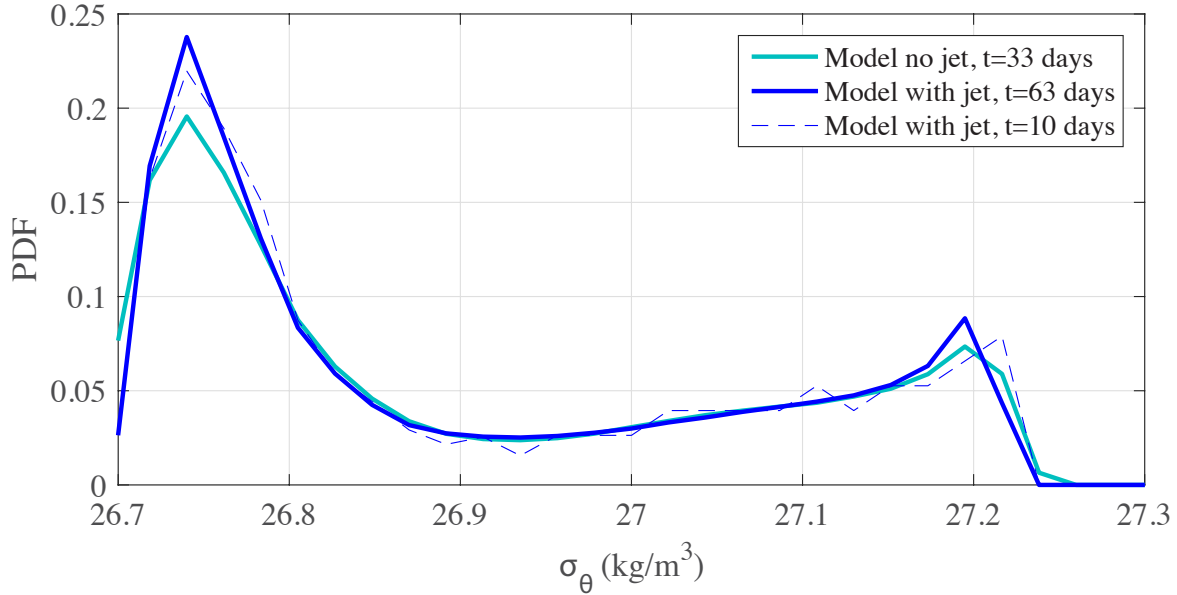
Figure S3: Probability density functions (PDFs) of potential density at the end of each simulation. For comparison, the same PDF is also plotted from the simulation with a jet at $t = 10$ days before submesoscale instabilities develop.

cold filament (see Fig. 1b in the main text and Fig. S3). These were called the 'outer front' and 'inner front', indicating their position relative to the center of the meander. The 'outer front' was associated with a larger temperature contrast, but due to partial compensation by salinity it had a smaller density contrast than the inner front. In order to test the sensitivity of the model subduction on the existence of a dense filament and strength of the fronts, two additional simulations were run with the inner front removed and with and without the ACC jet.

The calculation of the subduction volume from Fig. 5c of the main text was repeated for the new simulations and is shown in Fig. S4. The density class used to calculate the subducted volume in Fig. 5c is not present in the new simulations. Instead, the subduction volume was calculated for water with temperatures less than $1.5°C$. The same initial condition for temperature was used in all simulations (see Fig. 1b and Fig. S3), although since density is the dynamic variable in these simulations, temperature acts as a passive tracer. For comparison, the

7

subduction volume for the simulations in the main text with a dense filament are also shown.

The subduction volume for the simulations with just the outer front is significantly smaller than the corresponding simulations with a dense filament. Note that the change in density across the outer front is quite small, 0.052 kg/m^3, compared with 0.094 kg/m^3 across the inner front. Filaments are also known to be more susceptible to rapid sharpening (filamentogenesis) than fronts (frontogensis), see e.g. McWilliams, 2016. In the simulation with an outer front and an ACC jet (dashed blue line), the subduction takes place over a slightly longer time period than in the case with a dense filament. As a result of the smaller subducted volume and longer time interval over which subduction takes place, the subduction rate in the simulation with just the outer front and a jet is about 10 times smaller than the simulation with a dense filament and a jet.

Despite the differences in the magnitude of subduction, the presence of the ACC jet plays a similar role in the two sets of simulations. Specifically, in both sets of simulations subduction occurs more rapidly without a jet, but subduction is sustained for a longer period with a jet. In both cases, the net subducted volume is similar at the end of the simulations with and without a jet. One notable difference is that in the simulation with an outer front and no jet, the subducted volume decreases after reaching a maximum at about 20 days, indicating a period of upwelling. A brief period of downwelling occurs in the simulation with a filament and no front between 13-14 days, although the amplitude in terms of subducted volume is much smaller. The causes of the downwelling events is not clear.
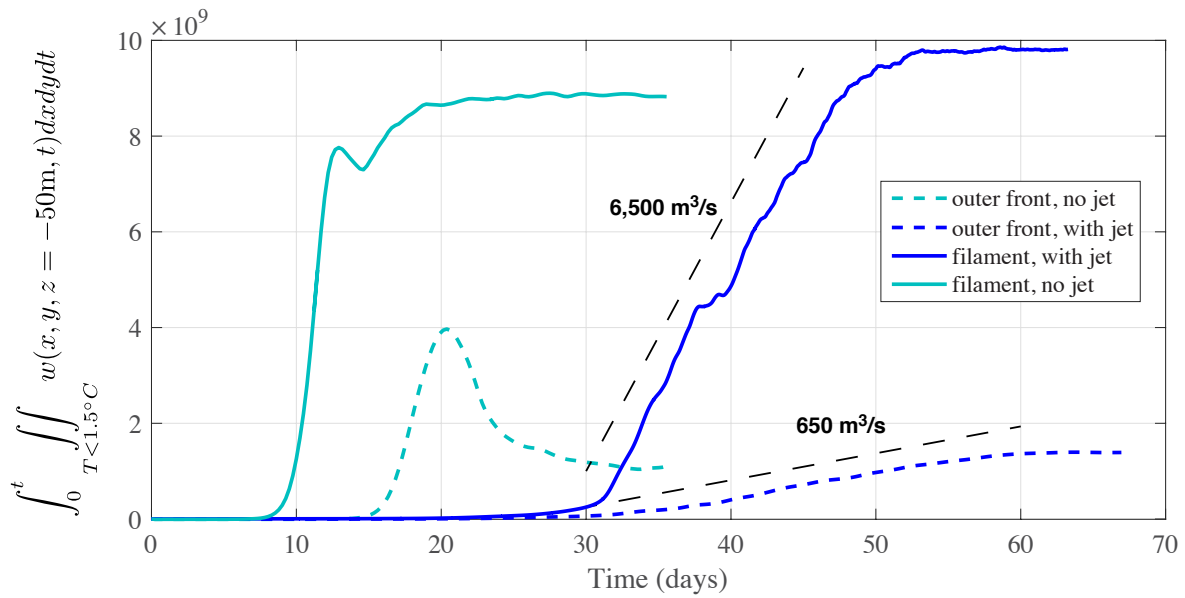
Figure S4: Subducted volume (units of m^3) for the simulations reported in the main text with two opposing fronts surrounding a dense filament, and two additional simulations with just the outer front present.